1 Thermodynamic analysis of dehydration of $K_2CO_3 \cdot 1.5H_2O$.

- 2 Authors: Natalia Mazur^{1,2} Henk Huinink^{1,2*}, Bart Borm¹, Stefano Sansota^{1,3}, Hartmut Fischer⁴, Olaf
- 3 Adan^{1,2,4}
- ⁴ Eindhoven University of Technology, Den Dolech 2, 5600 MB Eindhoven, The Netherlands.
- ² Eindhoven Institute for Renewable Energy Systems, Eindhoven University of Technology, PO Box
- 6 513, 5600 MB Eindhoven, The Netherlands
- 7 ³ CFM, University of the Basque Country, Paseo de Manuel Lardizabal, 5, 20018 Donostia-San
- 8 Sebastian, Gipuzkoa, Spain
- 9 ⁴TNO Materials Solutions, High Tech Campus 25, 5656 AE Eindhoven, The Netherlands
- 10 *h.p.huinink@tue.nl

Abstract

11

- 12 This work studied the reversible dehydration of potassium carbonate sesquihydrate ($K_2CO_3 \cdot 1.5H_2O$).
- 13 The study is based on isobaric and isothermal thermogravimetric measurements conducted at a
- 14 broad range of vapour pressures and temperatures. By controlling both parameters, we examined
- the influence of both constraints on the reaction kinetics at a wide extent of supersaturations. We
- 16 have evaluated our experimental findings by employing two thermodynamic theories, classical
- 17 nucleation theory and transition state theory. By combining both approaches, we were able to
- establish that: 1) At low supersaturations in a region close to equilibrium, dehydration is limited by
- 19 nucleation and growth of the anhydrous phase 2) At high supersaturations, dehydration reaches
- 20 maximum rate and is controlled by the reaction speed. Furthermore, we show that the dehydration
- 21 of K₂CO₃·1.5H₂O is very sensitive to pressure-temperature conditions and that it does not possess
- 22 universal activation energy.

Keywords

23

- Thermochemical energy storage, Classical nucleation theory, Transition state theory, Dehydration of
- 26 salts

27

24

25

1. Introduction

Dehydration properties of salt hydrates have been studied for decades, and with this, they have contributed significantly to the development of present theories of solid-solid phase transitions [1–3]. In recent years, the interest shifted from purely fundamental to application-oriented [4,5]. The interest in potassium carbonate sesquihydrate has followed similar development, where recently, it has been extensively studied as a thermochemical heat storage material [6–10]. The dehydration of $K_2CO_3 \cdot 1.5H_2O$ is a reversible process expressed as:

35
$$K_2CO_3\cdot 1.5H_2O(s) \rightleftharpoons K_2CO_3(s) + 1.5H_2O(g)$$
 (Rx. 1)

On a macroscopic scale, the process is schematically represented in Figure 1. During dehydration, a morphological change takes place in the crystal. When the water leaves the hydrate, a layer of solid anhydrous material forms on the surface. The thickness of that material will steadily increase with time till all material has dehydrated [11]. Water vapour, generated during the reaction, must therefore diffuse through pores and cracks in the anhydrous salt to escape the solid [7].

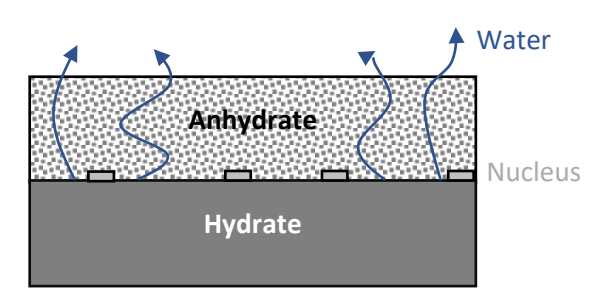


Figure 1 Scheme of dehydration

Early studies on the dehydration of $K_2CO_3 \cdot 1.5H_2O$ have suggested the existence of monohydrate [12] [13] or hemihydrate [14]; however, this was never fully confirmed [15,16]. The study by Stanish et al. [16] describes the dehydration process of $K_2CO_3 \cdot 1.5H_2O$ as a single step process of which the subsiding speed can be explained with the shrinking core model. This model describes reaction progress from outside of a particle towards its core, during which a shell of reacted material is formed, often causing diffusion issues. A similar model was used in the study by Gaeini [8], who investigated the influence of temperature and vapour pressure on reaction kinetics far from equilibrium conditions.

In addition to decreasing dehydration speed with increasing conversion, Stanish et al. have observed extremely slow kinetics close to equilibrium conditions. A similar drastic drop in dehydration rate was observed by Sögütoglu et al. [17]. They have mapped out an area close to equilibrium conditions, dubbed the metastable zone (MSZ), where no instantaneous dehydration occurs. Figure 2 illustrates the principle of this phenomenon, where the red line indicates the measured mass loss at 12 mbar vapour pressure when the temperature gradually increases from 25-105 °C. It shows a dormant period within the hatched area (MSZ), when temperature increases above the equilibrium line (thick black line) and when the dehydration starts (dashed line). This kind of hysteresis is not specific to potassium carbonate, as it has been observed in many other salt hydrates [18], and it is commonly associated with a nucleation barrier [19,20].

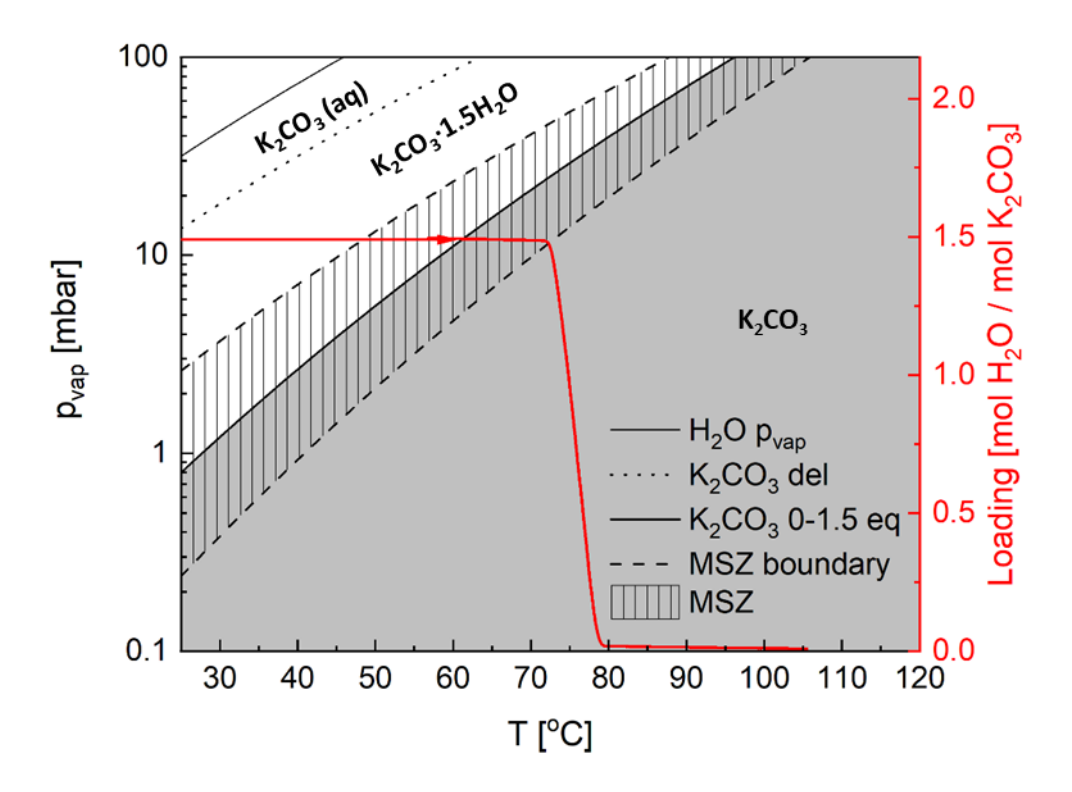


Figure 2 K_2CO_3 pressure-Temperature phase diagram adapted from [17]. p_{vap} is vapour pressure, and T is sample temperature. The red line shows the measured change in loading (right axis) at 12 mbar between 25-105°C and at 0.3°C/min heating rate.

Considering all the previous observations, we have noticed that the dehydration behaviour of $K_2CO_3 \cdot 1.5H_2O$ is strongly dependent on the vapour pressure and its relationship to the equilibrium line. Therefore, depending on the reaction conditions, different phenomena can be observed. Those phenomena can lead to a series of limitations to the reaction progress, such as nucleation barrier, diffusion limitation or reaction limitation.

The goal of this work is to reassess the dehydration behaviour of K_2CO_3 . Given the existence of two thermodynamically different zones, we aim to elucidate the influence of water vapour on the nature of dehydration at a wide range of conditions. Measurements are conducted at fixed isobaricisothermal points within and outside of MSZ. The obtained data are evaluated from a thermodynamic point of view by taking driving force into account.

2. Theory of dehydration

80 The general dehydration reaction can be described as:

81
$$S \cdot bH_2O(s) \underset{k_2}{\rightleftharpoons} S \cdot aH_2O(s) + (b-a)H_2O(g)$$
 (Rx.2)

where S is a salt unit, while b and a are the numbers of water molecules partaking in the reaction, and where b>a, and k_1 and k_2 are reaction rate constants for the forward and reverse reaction, respectively.

The Gibbs energy for the reaction, ΔG_r^{o} [J], is given as:

$$\Delta G_r^o = -RT ln \left(\frac{p}{p^o}\right) = \Delta H_r^o - T \Delta S_r^o \tag{1}$$

- where R is the gas constant [8.3145 J/K mol], T [K] is the absolute temperature, p [mbar] is the
- vapour partial pressure, p^0 is the standard pressure [1013 mbar], ΔH_r^o [J/mol] and ΔS_r^o [J/K mol] are
- 89 enthalpy and entropy of the reaction, respectively.
- The works of Sögütoglu et al. [17,21] have shown that there are two main areas, where reaction
- 91 proceeds differently: 1) inside MSZ an area around equilibrium conditions (hatched area in Figure
- 92 2) where any reaction is preceded by an induction period; 2) outside MSZ zone past MSZ boundary
- 93 (a plain grey area in Figure 2), where the reaction is instantaneous. Due to significant differences in
- 94 how the reaction proceeds in each area, they will be treated separately.

2.1 Dehydration inside the MSZ

- 96 Dehydration behaviour and the observed induction period in salt hydrates are commonly explained
- 97 through the classical nucleation theory (CNT). The induction period τ [s] is defined as the time, which
- 98 elapses between the achievement of supersaturation and the start of rapid desupersaturation due
- 99 to the growth of the nucleus past its critical size [22]. The induction period is stochastic, and it can be
- 100 expressed as [17]:

95

$$\tau \propto J^{-1} \tag{2}$$

- where $J[s^{-1}]$ is the nucleation rate, which can be expressed as an Arrhenius-like reaction rate
- 103 equation [17]:

$$J = \kappa \exp\left(-\frac{\Delta G^*}{k_B T}\right) \tag{3}$$

- where κ [s⁻¹] is a kinetic parameter, ΔG^* [J] is the nucleation barrier, and k_B [1.38 × 10⁻²³ J/K] is the
- 106 Boltzmann constant.
- Nucleation barrier ΔG^* is dependent on the size of the nucleus, interface between the nucleus and
- the mother phase, dictated by the interfacial tension y [J/m²], the nucleus shape, which could be a
- 2D disk or a 3D (hemi)sphere, described by the shape factor ω , as well as the driving force $\Delta\mu$. In
- general terms, the nucleation barrier can be expressed as [22]:

111
$$\Delta G^* = \Delta G_{bulk} + \Delta G_{surface} = \frac{V}{v} (b - a) \Delta \mu + \gamma A \tag{4}$$

- where $V [m^3]$ is the molecular volume of the cluster, $v [m^3]$ is the volume of a single dehydrated unit,
- and A [m²] is the area of the cluster.
- 114 The driving force $\Delta\mu$ is dependent on temperature and vapour pressure according to the following
- 115 relation:

$$\Delta \mu = \mu_{anh} - \mu_{hyd} = k_B T ln \left(\frac{p}{p_{eq}}\right) = k_B T ln(p^*)$$
 (5)

- where p_{eq} [mbar] is the equilibrium vapour pressure at a given temperature, and the relationship
- between the applied vapour pressure p and the equilibrium pressure is called the supersaturation,
- 119 p^* .
- Depending on the shape of the nucleus, the nucleation barrier can be expressed as:

121
$$2D: \Delta G^* = -\frac{h\pi v \gamma^2}{(b-a)k_B T ln(p^*)}$$
 (6)

122
$$3D: \Delta G^* = -\frac{\eta \pi v^2 \gamma^3}{[(b-a)k_B T ln(p^*)]^2}$$
 (7)

- where h [m] is the height of the nucleus and η is a shape factor where $\eta=8/3$ for hemisphere and
- η=16/3 for a sphere.
- 125 Complete derivations of those two relationships can be found in Supplementary information
- 126 Appendix A. What both equations illustrate is that the nucleation barrier and thus the nucleation
- rate is dependent on supersaturation p^* [20]:

$$J = \kappa \exp\left(\frac{\lambda}{[\ln(p^*)]^n}\right) \tag{8}$$

- where λ is a thermodynamic parameter that relates to ΔG^* , with n=1 or 2 reflecting the nucleus's
- shape for respectively 2D or 3D nucleation.
- 131 A close examination of Equation 8 reveals that a critical level of supersaturation, p*_{crit}, must be
- exceeded to have instantaneous nucleation [22]. At conditions where $p^* < p^*_{crit}$, nucleation will occur
- only after a certain induction period which can be related to the supersaturation as follows [17]:

$$\ln\left(\tau^{-1}\right) = \ln(\kappa) - \frac{\lambda}{\left[\ln\left(p^*\right)\right]^n} \tag{9}$$

136

2.2 Dehydration outside the MSZ

- Outside of the MSZ, the dehydration process is usually described as a single step reaction with
- conversion, $\frac{d\alpha}{dt}$, being dependent on temperature and pressure in accordance with:

$$\frac{d\alpha}{dt} = f(\alpha)k(T)h(p) \tag{10}$$

- Function $f(\alpha)$ describes conversion that could be conveyed according to one of the well-established
- models [23]. The temperature dependency, k(T), is often expressed in the form of the Arrhenius
- 142 equation:

$$k(T) = A \exp\left(\frac{-E_a}{RT}\right) \tag{11}$$

- where A is the preexponential factor, E_a is the apparent activation energy. The apparent activation
- energy is commonly extracted from reaction rate measurements at different temperatures using the
- van 't Hoff plot and the equation above. Nevertheless, very little attention is usually given to the
- 147 reaction conditions, being vapour pressure and temperature, and their relation to equilibrium
- 148 conditions. Moreover, the basic Arrhenius approach does not account for the entropic term of Gibbs
- 149 energy.
- In transition state theory (TST), the reaction rate r can be expressed as:

151
$$r = k_1 - k_2 \approx C \exp\left(\frac{-\Delta G_b^{\sharp}}{k_B T}\right) - C \exp\left(\frac{-\Delta G_a^{\sharp}}{k_B T}\right)$$
 (12)

- where C is a constant and $\Delta G^{\#}$ is the change in Gibbs energy between the initial state b state and the
- 153 transition state (TS) or final state a and TS. With further consideration of the forward and backward
- reactions (done in Supplementary information Appendix B), this relationship transforms into:

$$155 r = Cexp\left(-\frac{\Delta G_b^{\#}}{k_B T}\right) \left[1 - \left(\frac{p}{p_{eq}}\right)^{\nu}\right] (13)$$

- 156 where v = N(b a)
- 157 $\Delta G_b^{\#}$ is the free energy barrier for reactant b to transform to the transition state. Comparing
- 158 Equation 11 and Equation 13, we see similarities in the exponential term. However, TST underlines
- the importance of supersaturation $(p/p_{eq}=p^*)$ when determining the energy barrier, which is often
- neglected in the classical Arrhenius approach.
- 161 The influence of water vapour is often neglected, not only while extracting the Arrhenius parameters
- 162 [24], but also when considering the pressure dependency term h(p) in Equation 10, h(p). This
- oversight is quite frequent since many experiments are conducted under a constant flow of inert gas
- with the assumption that gasses produced during the reaction are removed from the reaction zone.
- 165 Thus, their influence on the kinetics is less likely to be treated [5,25].
- 166 When accounted for, pressure dependency is most commonly defined as [4,5,21,26]:

167
$$h(p) = 1 - \frac{p}{p_{eq}}$$
 (14)

- which is based on the assumption that the overall reaction rate of Reaction 2 is dependent on the
- difference between forward and reverse reaction and the vapour partial pressure of the gaseous
- 170 product according to [4]:

- 172 Another form of pressure dependence previously encountered in the dehydrogenation of metal
- 173 hydrides is [27–29]:

$$h(p) = p_{eq} - p \tag{16}$$

- 175 This relationship can be related to Fick's first law of diffusion and suggests that the reaction rate is
- 176 proportional to the difference between equilibrium pressure and partial vapour pressure.
- Other forms of pressure dependence, or combinations thereof, have been used in the
- literature [4,27,30–32]. However, because they are either purely empirical or modelling
- 179 results, they will not be considered in our analysis.

181

3. Materials and methods

- 182 K₂CO₃ used in this study was purchased from Sigma-Aldrich. The as-received powder was ground in
- pestle and mortar and sieved between 50-164 µm particle fraction. Approximately 5 mg of this
- 184 powder was then loaded into a 40 μL Mettler-Toledo standard aluminium pan without a lid, which
- 185 was then loaded into a thermogravimetric analyser (TGA).
- 186 Reaction kinetics were studied in TGA 851e by Mettler-Toledo, which is coupled with an external, in-
- house built humidifier. The devices operate with a nitrogen atmosphere at a fixed flow rate of 300
- 188 mL/min. The temperature of TGA was calibrated using an SDTA signal of melting points of
- naphthalene, indium, and zinc. The humidifier was calibrated by establishing deliquescence point of
- 190 LiCl·H₂O, K₂CO₃·1.5H₂O, MgCl₂·6H₂O and Mg(NO₃)₂·6H₂O salt hydrates at 25 °C [33].

Before investigating dehydration kinetics, the sample was subjected to 20 (de)hydration cycles to minimise the effects of initial powder morphology [6][34]. During the cycling, hydration was conducted at 30 $^{\circ}$ C and 12 mbar water vapour pressure, while dehydration was conducted at 125 $^{\circ}$ C and 0 mbar.

The dehydration measurements are into 1) isobaric-isothermal measurements within MSZ and 2) isobaric-isothermal measurements outside MSZ. The conditions at which all measurements were conducted are indicated in Figure 3.

In total, 14 isobaric-isothermal measurements were conducted inside MSZ (Red dots in Figure 3) that were used to evaluate reaction kinetics and 28 outside MSZ (Black squares in Figure 3). Six of those points are at the edge of MSZ to better understand reaction development over a wider range of vapour pressures at a fixed vapour pressure. All those measurements follow the same protocol, illustrated in Figure 4. First, the sample is fully dehydrated in-situ for 60 min at 130 °C and 0mbar. Subsequently, it is fully hydrated for 60 min at 40 °C and 19 mbar. Then, the temperature is adjusted to desired conditions, and the sample is equilibrated for 30 min at the selected temperature and 19 mbar vapour pressure. Only then humidity with desired water content is introduced to the system. This point marks t=0 for further analysis purposes. To pinpoint the exact conditions at which the measurement is conducted, measured sample temperature and applied vapour pressure are used for analysis.

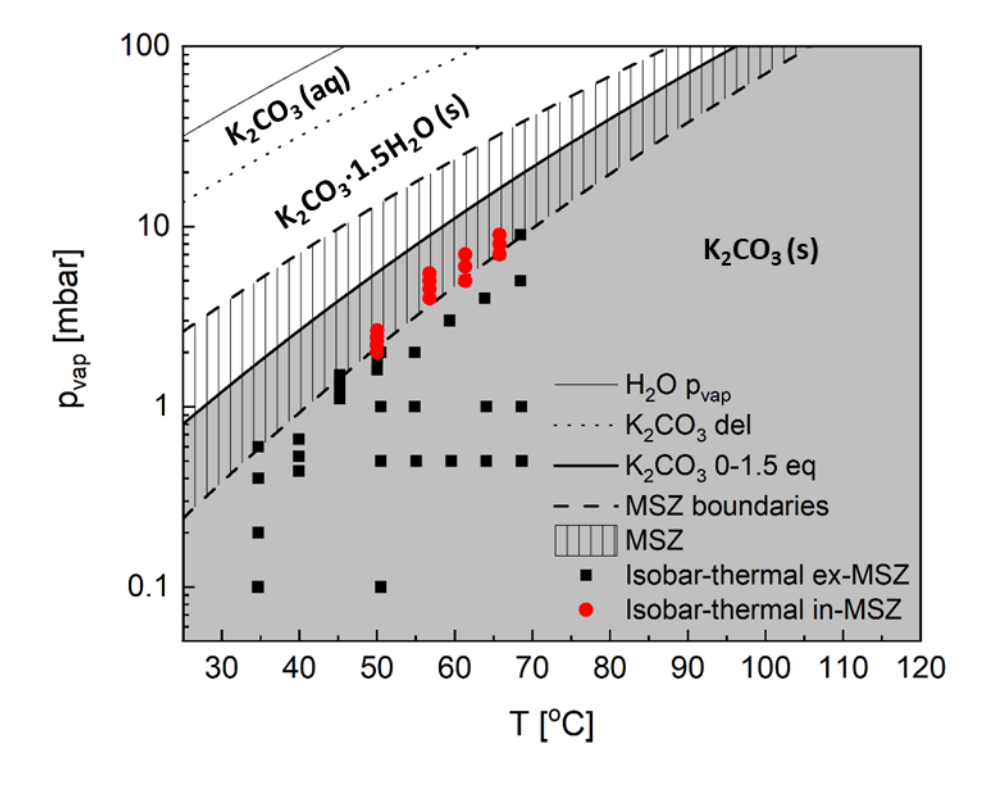


Figure 3 K_2CO_3 pressure-Temperature phase diagram adapted from [17]. p_{vap} is vapour pressure, and T is sample temperature. The equilibrium line between anhydrous and hydrated K_2CO_3 is drawn as a thick black line, and the dashed area indicates the metastable zone (MSZ). Red points indicate isobaric-isothermal kinetic measurements inside MZS, and black points indicate isobaric-isothermal kinetic measurements outside MZS.

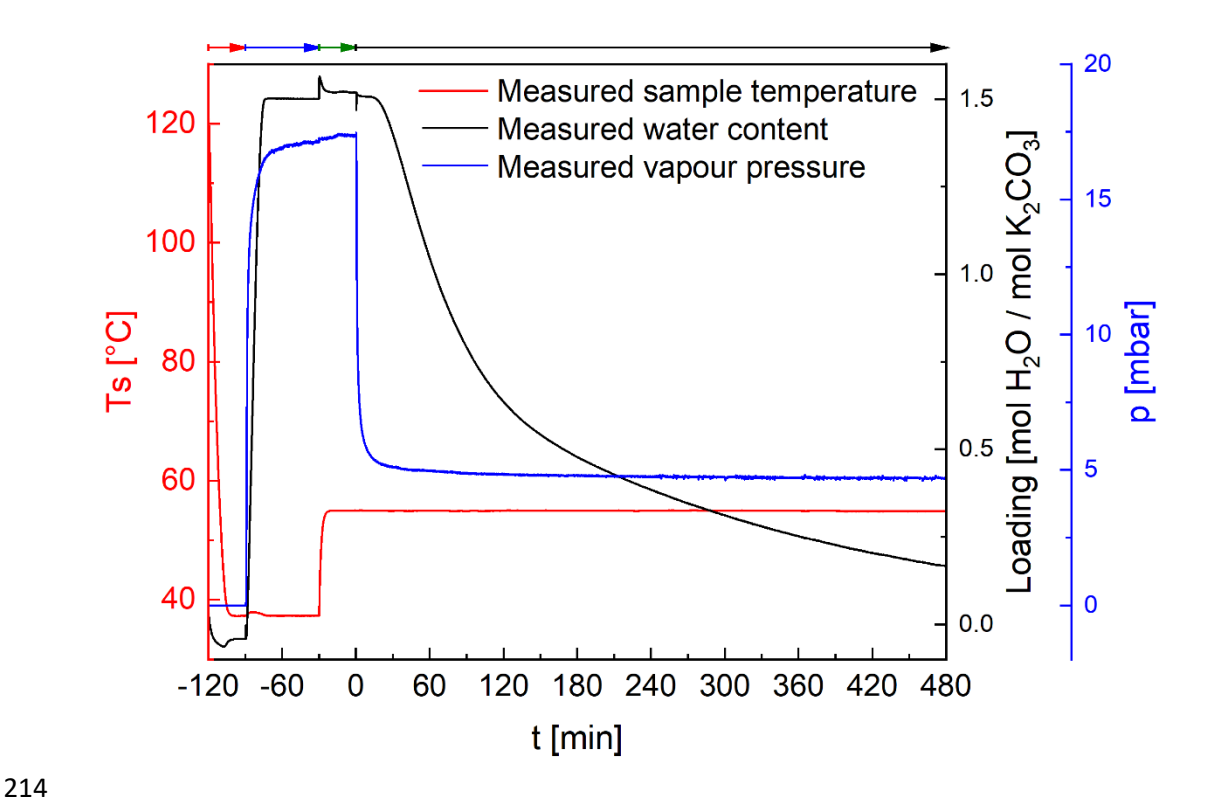


Figure 4 An example of measurement at isobaric-isothermal conditions at 57 °C and 5 mbar. The black plot shows calculated changes in loading based on the measured mass changes, the red plot is the measured sample temperature, and the blue plot is the measured vapour pressure at the outlet of the TGA. The red arrow indicates the dehydration period, the blue arrow indicates the hydration period, a green arrow indicates the settling period, and the black arrow indicates the

Ultimately, K_2CO_3 powder used in the TGA is investigated with scanning electron microscopy (SEM) to understand the morphology changes with dehydration and cycling. For this purpose, two powder samples were selected: a pristine K_2CO_3 powder that was ground and sieved identically as the samples for TGA analysis and a K_2CO_3 powder that was ground, sieved and subjected to 11 (de)hydration cycles in TGA. Before SEM imaging, powder samples were completely dehydrated in an oven at 130 °C. Samples were then fixed to a stub with carbon tape and immediately placed in the SEM to prevent any hydration. The images were taken with JEOL Fei Quanta 600. For the measurement high vacuum, 5 kV accelerating current and 3.0 spot size were used.

4. Results

measurement period.

4.1 The structure of uncycled and cycled K₂CO₃.

Since the morphology of K_2CO_3 particles changes with cycling, which can impact kinetics [3], we have investigated K_2CO_3 powder used in TGA measurements with SEM to get an impression of the morphology applicable to our study. In Figure 5 images obtained at 1000x magnification (top) and 5000x magnification (bottom) of uncycled (left) and cycled (right) are presented. The most important observation is the severe change in powder morphology with cycling. The uncycled powder has a fairly closed structure with very little porosity. After cycling, the surface area increases drastically, and more porosity is built into the material. At this point, it is hard to observe individual particles as many of them have merged into larger, interconnected agglomerates. The surface becomes much

rougher as pores and channels leading into the particle can be seen in many areas. Similar observations have been made in earlier studies investigating morphological changes of K_2CO_3 with cycling [7,34].

243 Uncycled Cycled

50µm 550µm

10µm

10µm

10µm

Figure 5 SEM images of uncycled powder (left) and cycled powder (right) of anhydrous K_2CO_3 at 1000x (top) and 5000x (bottom) magnification.

4.2 Dehydration kinetics within MSZ

Within the MSZ, we evaluate dehydration at a relatively high vapour pressure compared to equilibrium conditions. In this zone, the overall process is characterised by two attributes: 1) an induction period, τ , at the beginning of each measurement and 2) a subsequent reaction rate, as illustrated in Figure 6. The measurements within MSZ are conducted at four different temperatures (50, 57, 61 and 66 °C, red dots in Figure 3). Before a measurement starts, the sample is fully hydrated in situ at 40 °C and 19 mbar. Subsequently, the desired temperature is equilibrated for 30 min, after which the vapour pressure is lowered, and measurement begins.

From the measured data, we have determined the length of the induction period τ as the point of intersection between baseline at a stable loading of 1.5 mol H₂O/mol K₂CO₃ and a tangent at an inflexion point in the reaction rate curve (Red tangent lines on the dashed plot in Figure 6).

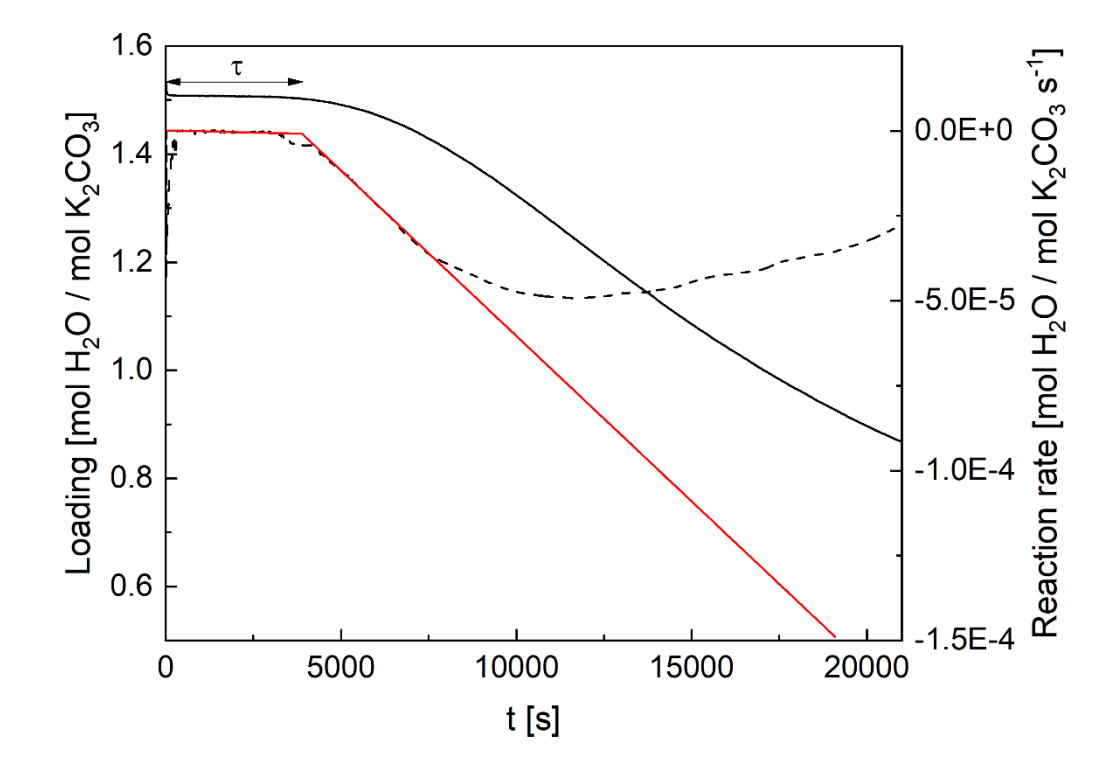


Figure 6 An example of induction time measurements at 57 °C and 5 mbar. The solid curve shows a change in loading, the dashed curve show change in dehydration rate vs time. The red tangents indicate the principle used to determine the length of an induction period.

The derived induction periods are summarised in Figure 7. This representation shows an exponential increase in the duration of the induction period with increasing pressure at a fixed temperature. A similar correlation has been observed previously for K_2CO_3 hydration [17] and many other salt hydrates [5,35,36]. The presence of an induction period is linked to CNT [20]. It is often explained as the time required for a nucleus to form and to start growing, which manifests itself as mass loss in our measurements.

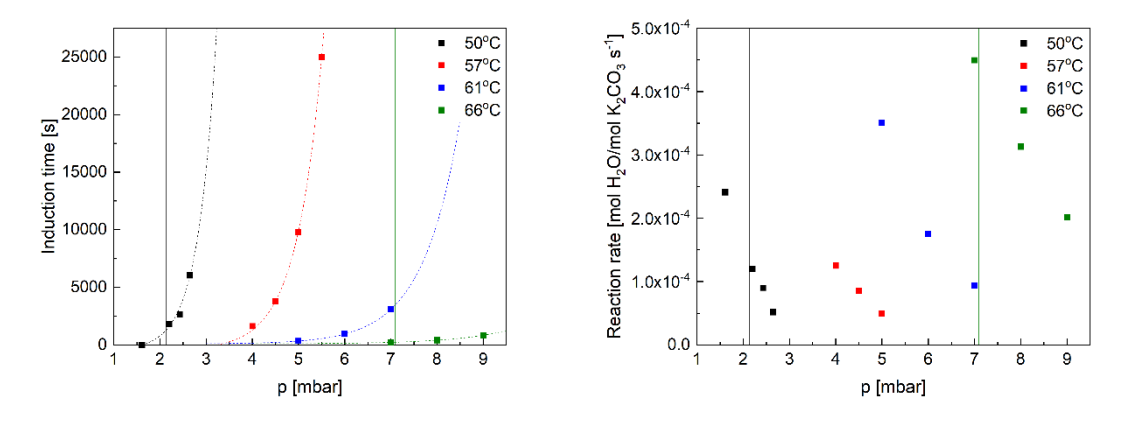
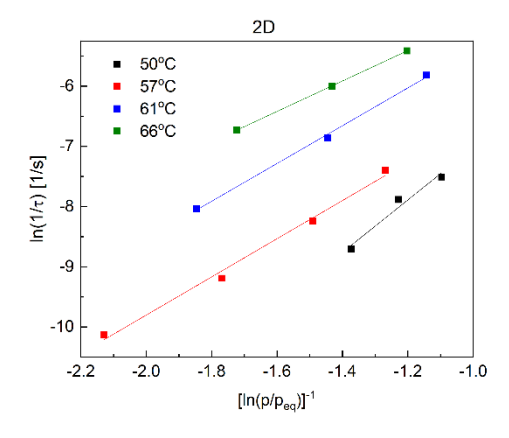


Figure 7 Measured a) induction period and b) reaction rates at isobaric-isothermal conditions at four different temperatures $(50\,^{\circ}\text{C} - black, 57\,^{\circ}\text{C} - red, 61\,^{\circ}\text{C} - blue, 66\,^{\circ}\text{C} - green})$. The solid lines indicate the edge of MSZ for the respective temperatures. The dashed lines connecting the points are just a guide for the eye. Note that most of the measurement time at $57\,^{\circ}\text{C}$ and $5.5\,$ mbar was consumed by the induction period; therefore, the reaction rate could not be measured.

The applicability of CNT for this case can be tested through the relationship presented in Equation 9. Here a linear correlation between inverse induction time and supersaturation is expected. In Figure 8, we see that such a relationship does indeed exist for each investigated temperature in both models. This means that the explanation for the dehydration process provided by CNT is appropriate within the MSZ. From this relation, we can extract surface tensions, γ , which vary between 9 mJ/m² for 3D nucleus to 22 mJ/m² for 2D nucleus, comparable with previously published values [17].



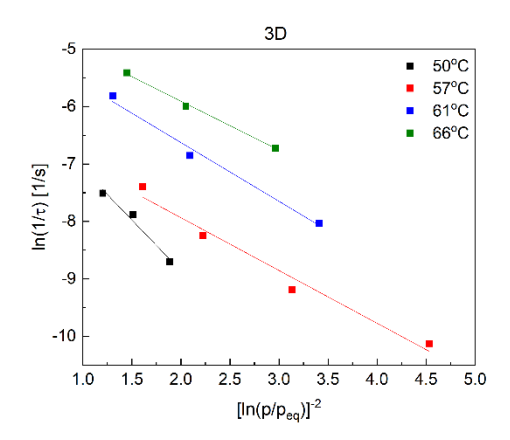


Figure 8 Measured inverse induction time vs $(\ln(p/p_{eq}))^n$ at different temperatures (50 °C – black, 57 °C – red, 61 °C – blue, 66 °C – green) according to Equation 9, together with linear fits assuming a) 2D nucleation and b) 3D nucleation.

A further evaluation of induction periods and their relationship with the dehydration rate is done in Figure 9, which gives us an insight into the growth process which occurs right after nucleation. We observe a nearly linear relationship between the maximum dehydration rate and the inverse induction time. At a fixed temperature, the reaction rate increases with decreasing induction time, which shows that within MSZ, nucleation of the anhydrous phase limits the reaction rate [17].

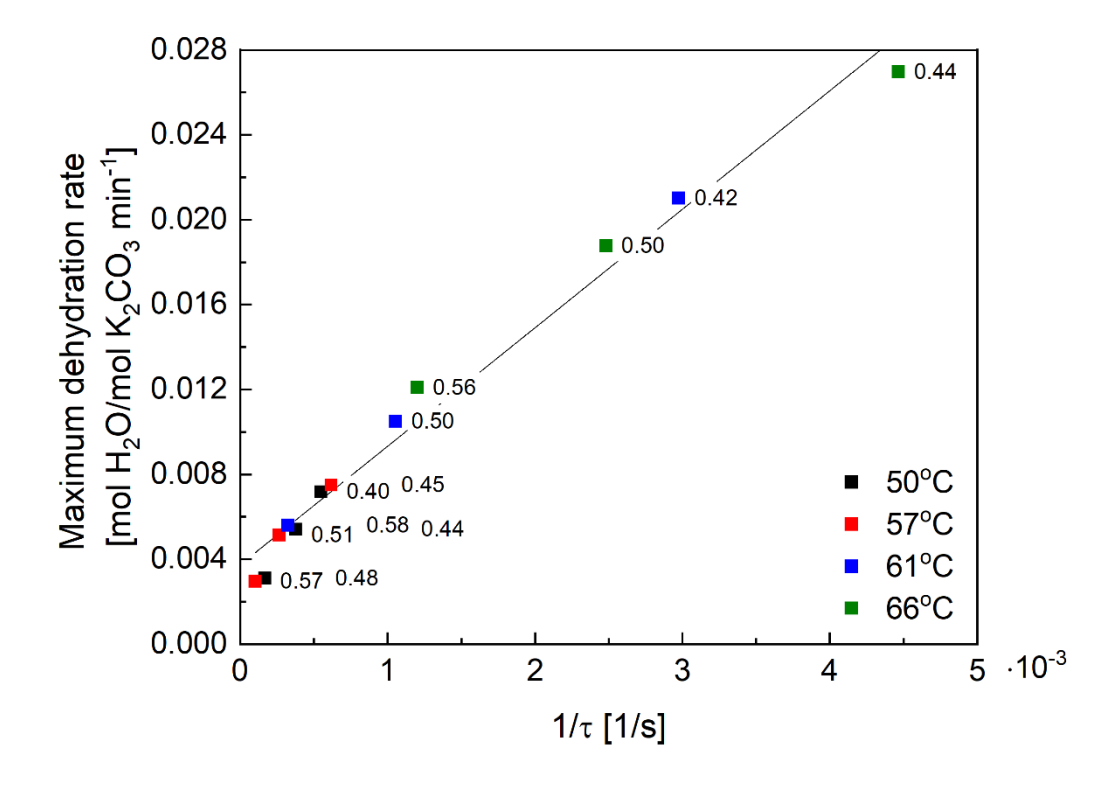
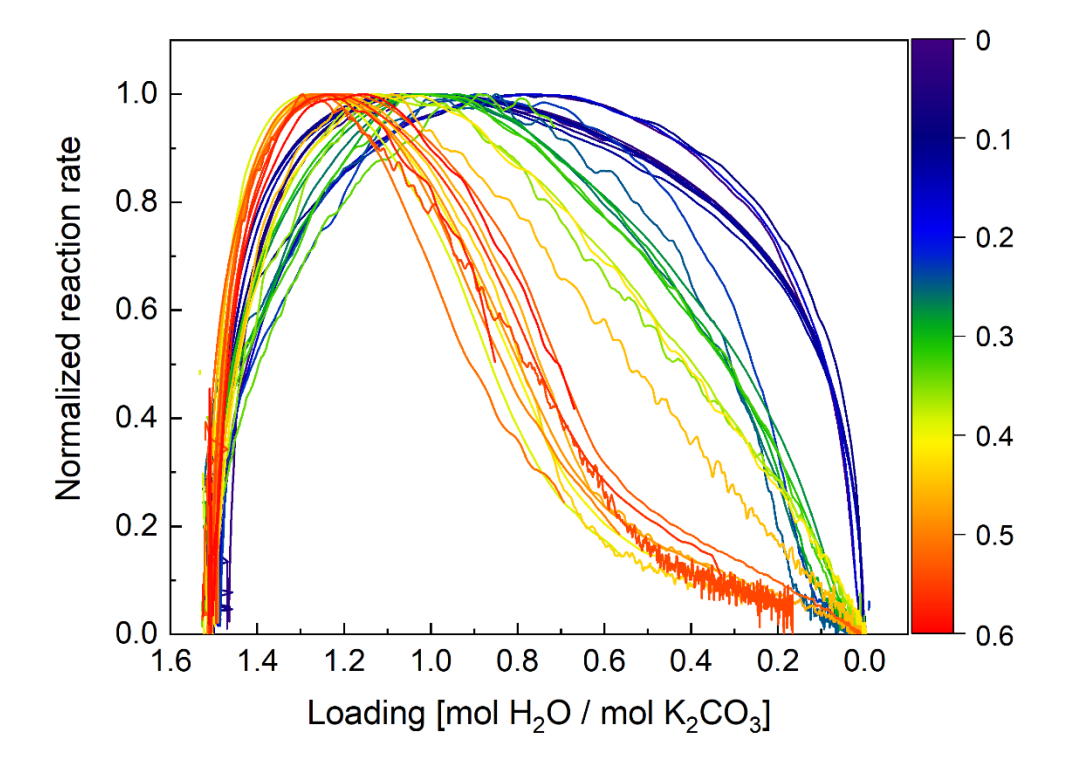
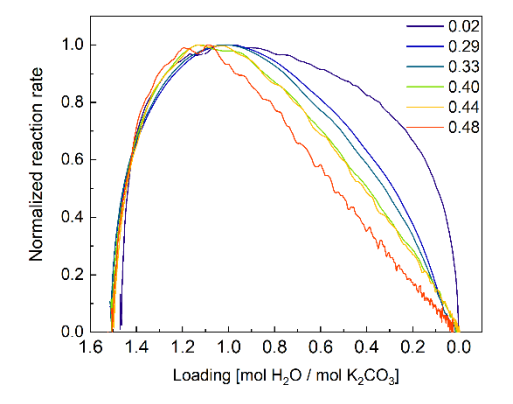


Figure 9 Maximum dehydration rates inside MSZ at four different temperatures ($50\,^{\circ}\text{C}$ – black, $57\,^{\circ}\text{C}$ – red, $61\,^{\circ}\text{C}$ – blue, $66\,^{\circ}\text{C}$ – green) as a function of the inverse induction time. p^* for the measurement is indicated as a label next to the data point, while the thin black line is a linear fit of the data.

4.3 Dehydration pathways

In the previous section, we have considered only the maximum dehydration rate in our evaluation in Figure 9, but this does not provide the entire picture. Considering the change in reaction rate as a function of loading, as illustrated on the top of Figure 10, we can see a trend developing. At high supersaturations, meaning far from MSZ, the reaction rate is relatively constant throughout the entire process, indicating a predominantly reaction limited dehydration process. As we move closer to the MSZ, the reaction rate drops off at much higher loading (lower conversion), ranging from 1 to 1.2 mol H_2O / mol K_2CO_3 . If we consult the corresponding loading vs time curves on the bottom of Figure 10, we observe increasing tailing in the mass loss. Those differences in dehydration pathways indicate that different processes limit the process at different supersaturation ranges.





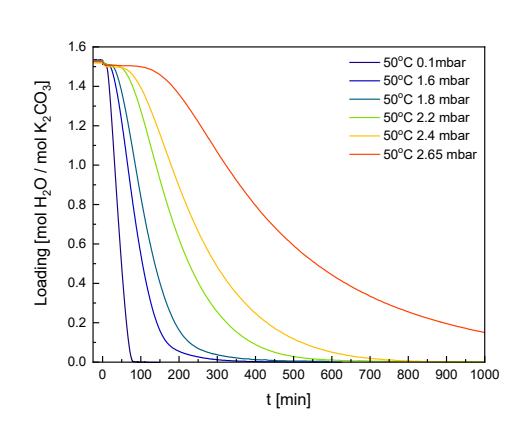


Figure 10 Top: Reaction rate plots normalised to the maximum rate as a function of loading colour coded according to p^* indicated in the legend. Bottom: Example of analysis on data collected at 50 °C and different p_{vap} a) Normalised reaction rate as a function of loading with p^* indicated in the legend b) Corresponding loading as a function of time with vapour pressures shown in the legend.

4.4 Dehydration kinetics

Based on the evaluation of reaction pathways inside and outside the MSZ, we have determined that dehydration of K_2CO_3 powder is reaction limited. It means that the activation energy E_a can be extracted through TST and Arrhenius analysis. In Figure 11, we plotted the maximum dehydration rates and colour-coded them according to p^* , which is also indicated in the label. Lyakhov [24] have postulated that the assumption of a linear relationship between reaction rate and 1000/T in the Arrhenius equation is valid only in a narrow p-T range or at comparable p^* values ($p^* \pm 0.02$). With this in mind, we have selected several narrow p^* zones to calculate the apparent activation energy. The resulting linear fits show that the apparent activation energy decreases with increasing driving

force and levels off at 78.5 kJ/mol when $p^* < 0.1$, also presented in the insert in Figure 11 as $1/p^*$. Those observations agree with remarks made by Lyakhov [24] and observations made by Galway [37], showing that there is no universal activation energy for a dehydration process but that it is strongly dependent on the reaction conditions. Furthermore, the values obtained outside MSZ are comparable with the activation energies reported in earlier studies which were in the range of 78.3-92 kJ/mol [8,16], [12], which is, as expected, somewhat higher than the reaction enthalpy 65.8 kJ/mol [6].

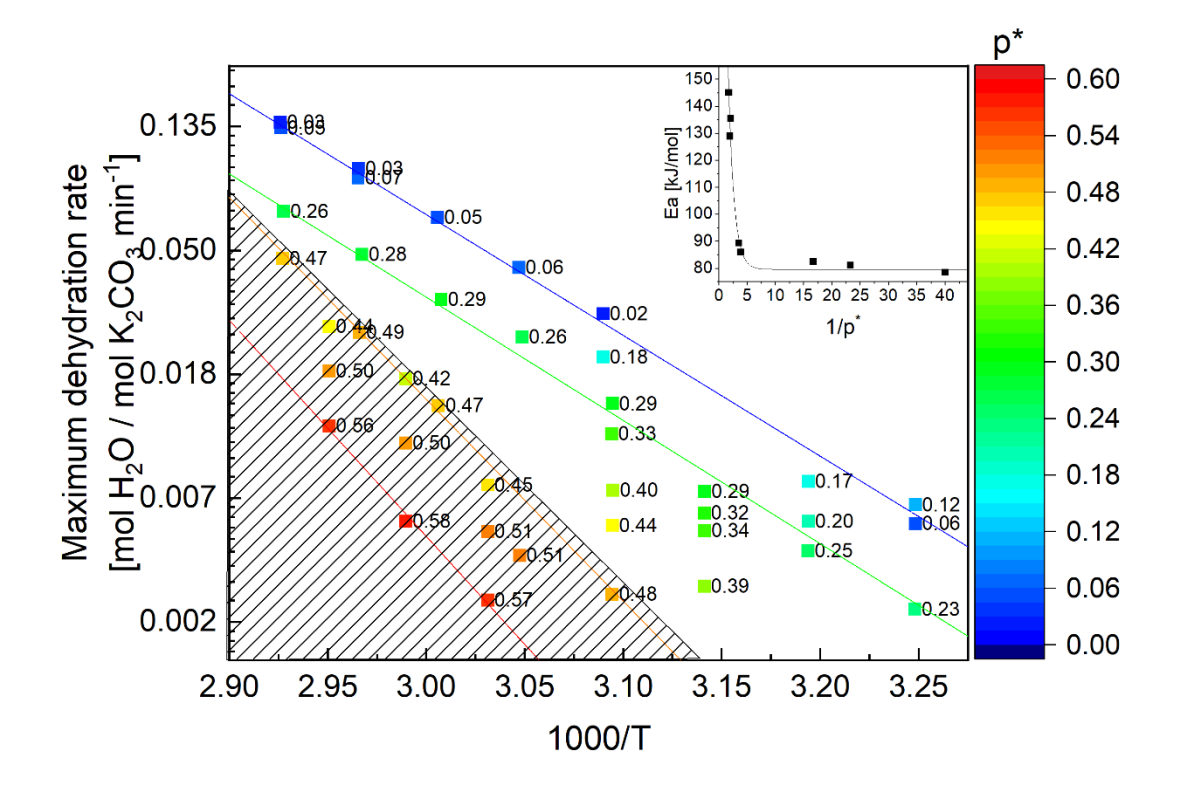


Figure 11 Arrhenius type plot based on maximum reaction rate at isobaric and isothermal conditions. Hatched area indicates MSZ, data points are colour coded according to p^* , and colour lines show linear fit used to calculate apparent activation energies shown in the insert as a function of $1/p^*$.

If we then consider the reaction rate as a function of supersaturation, as we did in Figure 12a, we see a linear relationship between the maximum reaction rate and p^* for each temperature. However, as we increase the supersaturation, the effect of vapour pressure on the dehydration rate decreases, as shown in Figure 12b. In addition, we notice that the maximum reaction rate stabilises for $1/p^* > 10$, which corresponds with the findings for stabilisation of E_a for $1/p^* > 8$ in Figure 11.

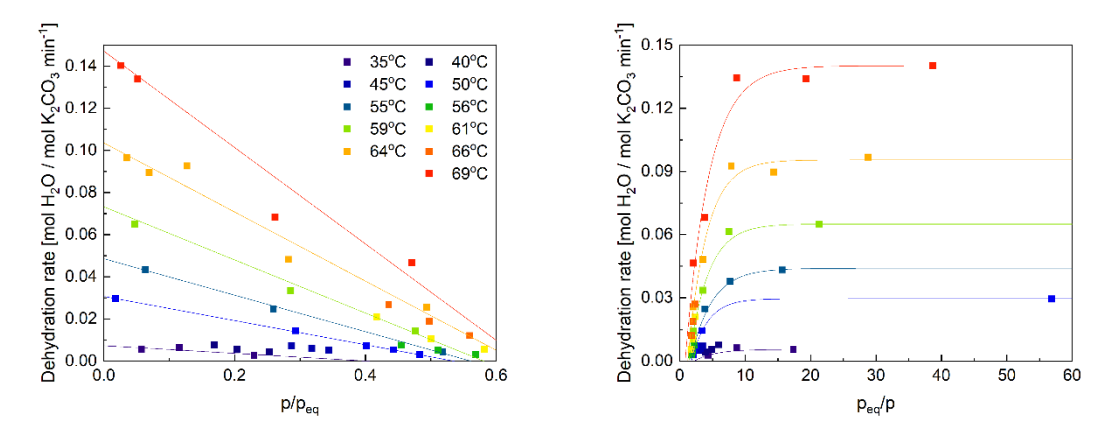


Figure 12 Dehydration rate as a function of a) supersaturation (p/p_{eq}) and b) inverse supersaturation (p_{eq}/p) at different temperatures.

To see if describing the reaction rate as a function of p^* , we have normalised reaction rates with E_a = 78.5 kJ/mol as shown in Figure 13. The presented plot gives a nearly linear relationship with respect to supersaturation, showing that the used approach is correct. The slight spread in the values and nonlinearity comes from variations in v in Equation 13. It is commonly set to 1, yet that does not have to hold for this case if it is, for example, a multistep process.

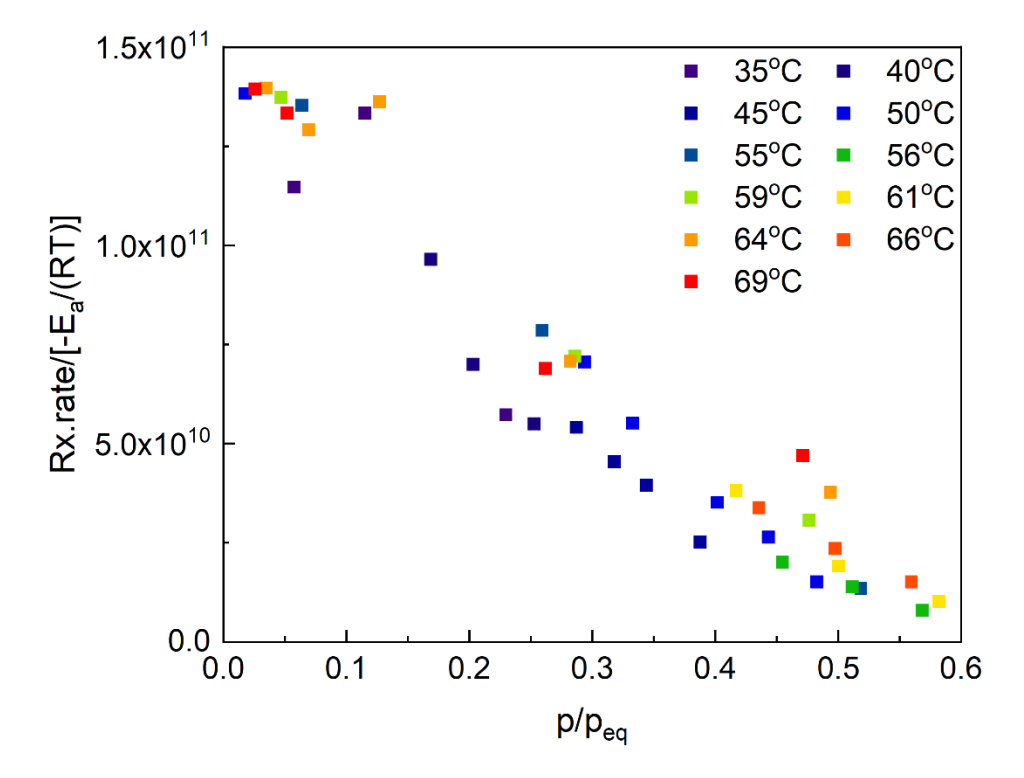


Figure 13 A master curve describing maximum dehydration rate normalised with the calculated activation energy $E_a = 78.5$ kJ/mol as a function of p^* .

5. Discussion

346

387

388

389

347 In this study, we have conducted a series of isobaric-isothermal measurements within and outside of 348 MSZ. Each measurement within MSZ begins with an induction period, meaning that although 349 thermodynamically, the conditions are suitable for dehydration to take place, it does not occur 350 immediately. This presence of the induction period implies several things. Firstly, close to 351 equilibrium conditions, the reaction is limited by nucleation, as shown in Figure 9. Secondly, the 352 dehydration behaviour in this region can be explained with the aid of CNT. Thirdly, the apparent 353 activation energies within MSZ, obtained in Figure 11, are a compound of the activation energy for 354 the reaction and the added threshold in from of nucleation barrier, which increases with increasing 355 proximity to the equilibrium conditions, resulting in elevated E_a values. 356 Outside of MSZ, dehydration is no longer limited by the nucleation of the anhydrous phase but by 357 the reaction itself. This is, on the one hand, inferred from Error! Reference source not found., where 358 the reaction rate is nearly constant throughout the entire process, while on the other hand, it 359 becomes insensitive to supersaturation when p* < 0.1, as shown in Figure 11 360 Finally, if we evaluate dehydration pathways at different supersaturations, we see that the reaction 361 might not be a single-step process as it is commonly believed. In Error! Reference source not found., 362 we see that as the supersaturation decreases, a clear maximum in the dehydration rate at 363 approximately 33% of conversion appears, which is followed by a gradual decrease in the reaction 364 rate. There are two possible reasons for that kind of behaviour: diffusion limitation or reaction 365 limitation. Typically, this behaviour is described with the aid of a shrinking core model, which could 366 give rise to diffusion limitation during dehydration [8,16]. However, if the dehydration far outside 367 the MSZ is principally reaction limited, the same should apply to a broader range of 368 supersaturations. However, as we move into MSZ, the driving force for dehydration becomes 369 insufficient for the entire process to proceed at a constant rate suggesting a multistep process taking 370 place. 371 There are indications in early literature that dehydration of K₂CO₃·1.5H₂O is a multistep process. In 372 their study, Deshpande et al. [12] showed that K₂CO₃ dehydrates in 2 steps of 0.5 and 1 mol of H₂O, 373 each with its own activation energy. However, they did point out that the calculated activation 374 energy depends on the measurement conditions and the assumptions made during the calculations, 375 a factor that has not been accounted for by Stanish et al. [16] or Gaeini et al. [8]. Furthermore, they 376 have postulated that dehydration of K₂CO₃ crystals is a nucleation and growth process, which agrees 377 well with our own observations. Interestingly, the thermodynamic equilibrium line for K₂CO₃ 0 - 0.5 378 H₂O transition, based on values obtained by Thomsen [14,38], coincides well with the more recently 379 established MSZ boundary for dehydration [17]. Therefore, although there is no conclusive evidence 380 for the existence of lower hydrates of K₂CO₃, we cannot exclude a metastable hydration state. 381 To evaluate the possibility of multistep dehydration, we take a closer look at the crystal structure of 382 K₂CO₃·1.5H₂O, shown in Figure 14. At first glance, all water molecules seem to be arranged in a single 383 plane. However, a closer investigation shows that we potentially have two different environments 384 within that plane. The black circle in Figure 14 marks the first environment that includes $\frac{1}{3}$ of those 385 molecules, which form a single file through the structure. The green circles mark the remaining $^2/_3$ of 386 water molecules, which are arranged as a double file of two channels mirroring each other. If we

compare that with the consistent dehydration maximum at approximately 1mol H₂O / mol K₂CO₃ in

Error! Reference source not found., we see that $\frac{1}{3}$ of water molecules is released easier or faster

than the remaining $^2/_3$. Such a process does not have to involve a new crystal phase in K_2CO_3 .

Nevertheless, a metastable phase of $K_2CO_3 \cdot H_2O$ or $K_2CO_3 \cdot 0.5H_2O$ that requires a higher energy input could be formed.

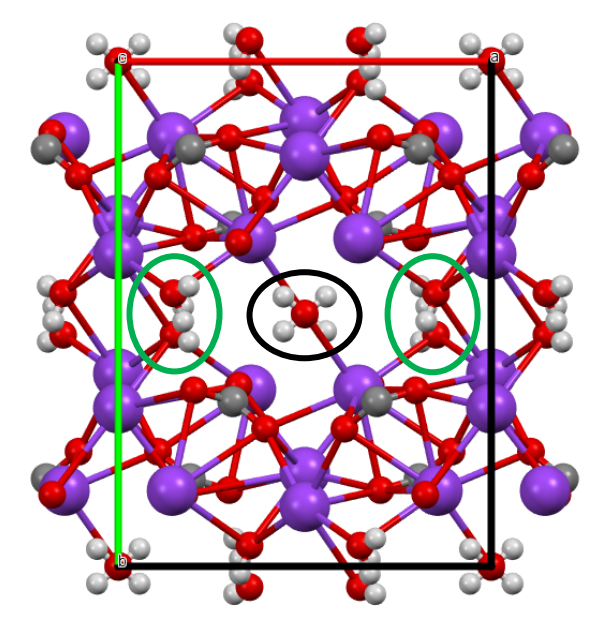


Figure 14 Crystal structure of K_2CO_3 ·1.5 H_2O , showed along c-axis, based on ICSD-280789 and generated in Mercury software. The unit cell axes are a-red and b-green. The atom colours are: potassium-purple, carbon-grey, oxygen-red and hydrogen-white. The $^1/_3$ of water molecules forming a channel through the structure are marked with a black circle. The remaining $^2/_3$ or water molecules are marked with a green circle.

6. Conclusion

In this work, we have evaluated the effect of water vapour pressure on the dehydration behaviour of $K_2CO_3 \cdot 1.5H_2O$. Through a series of isobaric-isothermal measurements at fixed points close to the equilibrium conditions, we have established that within MSZ, the reaction is limited by the nucleation rate, and the process can be explained through CNT. The nucleation barrier disappears when the MSZ boundary is crossed, and the reaction begins instantaneously. In this region, the rate is limited by the reaction speed itself. Nevertheless, a sufficiently low supersaturation must be provided for the reaction to proceed at a constant rate. It has been estimated that for $p^* < 0.1$, both reaction rate and apparent activation energy are relatively constant and do not change with decreasing p^* . If the supersaturation is not sufficiently low, the dehydration rate seemingly proceeds in two or three steps, and it is limited by the removal of the last 0.5 mol of H_2O . To verify this theory, a thorough investigation with atomistic simulations should be conducted. Based on our experimental work, we can conclude that dehydration of K_2CO_3 is a multistep process, whose activation energy is strongly dependent on reaction conditions and where water vapour plays a crucial role.

Acknowledgements

- This publication is part of the project Mat4Heat with project number 739.017.014 of the research programme Mat4Sus which is financed by the Dutch Research Council (NWO).
- The authors thank Hans Dalder op for his technical support.

117	Bib	liogra	phy

- 418 [1] B. Topley, M.L. Smith, Function of Water Vapour in the Dissociation of a Salt Hydrate, Nat. 1931 1283225. 128 (1931) 302–302. https://doi.org/10.1038/128302a0.
- 420 [2] B.J. Colvin, J. Hume, T H E DEHYDRATION O F SALT HYDRATES, J. Anzer. Chem. Soc. (1916) 421 2263.
- T.B. Benjamin, M.J. Lighthill, Nucleation phenomena arising during the dehydration of solid hydrates, Proc. R. Soc. London. Ser. A. Math. Phys. Sci. 224 (1954) 460–471. https://doi.org/10.1098/rspa.1954.0173.
- 425 [4] S. Vyazovkin, Kinetic effects of pressure on decomposition of solids, 426 Https://Doi.Org/10.1080/0144235X.2019.1691319. 39 (2019) 35–66. 427 https://doi.org/10.1080/0144235X.2019.1691319.
- G.D. Preturlan, L. Vieille, S. Quiligotti, L. Favergeon, J.G.D. Preturlan, L. Vieille, S. Quiligotti, L. Favergeon, Kinetics and Mechanism of the Dehydration of Calcium Sulfate Dihydrate: A
 Comprehensive Approach for Studying the Dehydration of Ionic Hydrates under Controlled
 Temperature and Water Vapor Pressure, 124 (2020) 26352–26367.
 https://pubs.acs.org/doi/full/10.1021/acs.jpcc.0c09041 (accessed June 4, 2021).
- 433 [6] L.C. Sögütoglu, P.A.J. Donkers, H.R. Fischer, H.P. Huinink, O.C.G. Adan, In-depth investigation 434 of thermochemical performance in a heat battery: Cyclic analysis of K2CO3, MgCl2and Na2S, 435 Appl. Energy. 215 (2018) 159–173. https://doi.org/10.1016/j.apenergy.2018.01.083.
- 436 [7] M.A.J.M. Beving, A.J.H. Frijns, C.C.M. Rindt, D.M.J. Smeulders, Effect of cycle-induced crack 437 formation on the hydration behaviour of K2CO3 particles: Experiments and modelling, 438 Thermochim. Acta. 692 (2020) 178752. https://doi.org/10.1016/j.tca.2020.178752.
- 439 [8] M. Gaeini, S.A. Shaik, C.C.M. Rindt, Characterisation of potassium carbonate salt hydrate for 440 thermochemical energy storage in buildings, Energy Build. 196 (2019) 178–193. 441 https://doi.org/10.1016/j.enbuild.2019.05.029.
- 442 [9] A.I. Shkatulov, J. Houben, H. Fischer, H.P. Huinink, Stabilisation of K2CO3 in vermiculite for thermochemical energy storage, Renew. Energy. 150 (2020) 990–1000. https://doi.org/10.1016/j.renene.2019.11.119.
- 445 [10] K. Kant, A. Shukla, D.M.J. Smeulders, C.C.M. Rindt, Performance analysis of a K2CO3-based 446 thermochemical energy storage system using a honeycomb structured heat exchanger, J. 447 Energy Storage. 38 (2021) 102563. https://doi.org/10.1016/J.EST.2021.102563.
- 448 [11] A.K. Galwey, Structure and order in thermal dehydrations of crystalline solids, Thermochim. Acta. 355 (2000) 181–238. https://doi.org/10.1016/S0040-6031(00)00448-2.
- 450 [12] D.A. Deshpande, K.R. Ghormare, N.D. Deshpande, A. V Tankhiwale, DEHYDRATION OF CRYSTALLINE K2C03-1.5 H2O, 66 (1983) 255–265.
- 452 [13] J.J. Pohl, Chemische Notizen, J. Für Prakt. Chemie. 82 (1861) 148–170.
 453 https://doi.org/10.1002/PRAC.18610820120.
- 454 [14] J. Thomsen, Thermochemische Untersuchungen. XXVIII. Ueber die Constitution der 455 wasserhaltigen Salze, J. Für Prakt. Chemie. 18 (1878) 1–63. 456 https://doi.org/10.1002/PRAC.18780180101.
- 457 [15] A.E. Hill, Hydrated potassium sesquicarbonate, K2CO3·2KHCO3·3/2H2O, J. Am. Chem. Soc. 52 (1930) 3817–3825. https://doi.org/10.1021/ja01373a008.

- 459 [16] M.A. Stanish, D.D. Perlmutter, Kinetics and transport effects in the dehydration of crystalline 460 potassium carbonate hydrate, AIChE J. 29 (1983) 806–812. 461 https://doi.org/10.1002/aic.690290515.
- 462 [17] L.C. Sögütoglu, M. Steiger, J. Houben, D. Biemans, H.R. Fischer, P. Donkers, H. Huinink, O.C.G.
 463 Adan, Understanding the Hydration Process of Salts: The Impact of a Nucleation Barrier,
 464 Cryst. Growth Des. 19 (2019) 2279–2288. https://doi.org/10.1021/acs.cgd.8b01908.
- 465 [18] M. Richter, E.M. Habermann, E. Siebecke, M. Linder, A systematic screening of salt hydrates 466 as materials for a thermochemical heat transformer, Thermochim. Acta. 659 (2018) 136–150. 467 https://doi.org/10.1016/j.tca.2017.06.011.
- 468 [19] A.K. Galwey, M.E. Brown, Thermal decomposition of ionic solids: chemical properties and reactivities of ionic crystalline phases, Elsevier, 1999.
- W.J. Dunning, Nucleation and Growth Processes in the Dehydration of Salt Hydrate Crystals, Kinet. React. Ion. Syst. c (1969) 132–155. https://doi.org/10.1007/978-1-4899-6461-8_7.
- 472 [21] L.C. Sögütoglu, F. Birkelbach, A. Werner, H. Fischer, H. Huinink, O. Adan, Hydration of salts as a two-step process: Water adsorption and hydrate formation, Thermochim. Acta. 695 (2021). https://doi.org/10.1016/j.tca.2020.178819.
- 475 [22] J.W. Mullin, Crystallization, Elsevier, 2001.
- 476 [23] S. Vyazovkin, A.K. Burnham, J.M. Criado, L.A. Pérez-Maqueda, C. Popescu, N. Sbirrazzuoli,
 477 ICTAC Kinetics Committee recommendations for performing kinetic computations on thermal
 478 analysis data, Thermochim. Acta. 520 (2011) 1–19.
 479 https://doi.org/10.1016/j.tca.2011.03.034.
- 480 [24] N. Lyakhov, M. Maciejewski, A. Reller, Theoretical considerations on the temperature and 481 pressure dependence of the kinetics of reversible thermal decomposition processes of solids, 482 J. Solid State Chem. 58 (1985) 398–400.
- 483 [25] M. Deutsch, F. Birkelbach, C. Knoll, M. Harasek, A. Werner, F. Winter, An extension of the NPK 484 method to include the pressure dependency of solid state reactions, Thermochim. Acta. 654 485 (2017) 168–178. https://doi.org/10.1016/j.tca.2017.05.019.
- 486 [26] A. Fopah Lele, F. Kuznik, H.U. Rammelberg, T. Schmidt, W.K.L. Ruck, Thermal decomposition 487 kinetic of salt hydrates for heat storage systems, Appl. Energy. 154 (2015) 447–458. 488 https://doi.org/10.1016/j.apenergy.2015.02.011.
- 489 [27] P.D. Goodell, P.S. Rudman, Hydriding and dehydriding rates of the LaNi5-H system, J. Less Common Met. 89 (1983) 117–125. https://doi.org/10.1016/0022-5088(83)90255-2.
- 491 [28] T. Hirata, T. Matsumoto, M. Amano, Y. Sasaki, Dehydriding reaction kinetics in the improved intermetallic Mg2Ni2H system, J. Less Common Met. 89 (1983) 85–91.
 493 https://doi.org/10.1016/0022-5088(83)90252-7.
- 494 [29] L. Belkbir, E. Joly, N. Gerard, A kinetic study of the LaNi4.9Al0.1-H2 system, J. Less Common 495 Met. 81 (1981) 199–206. https://doi.org/10.1016/0022-5088(81)90026-6.
- 496 [30] Y. Yamamoto, L. Favergeon, N. Koga, Thermal Dehydration of Lithium Sulfate Monohydrate
 497 Revisited with Universal Kinetic Description over Different Temperatures and Atmospheric
 498 Water Vapor Pressures, J. Phys. Chem. C. 124 (2020) 11960–11976.
 499 https://doi.org/10.1021/ACS.JPCC.0C02739.
- 500 [31] Satoki Kodani, Shun Iwasaki, Loïc Favergeon, Nobuyoshi Koga, Revealing the effect of water 501 vapor pressure on the kinetics of thermal decomposition of magnesium hydroxide, Phys.

502		Chem. Chem. Phys. 22 (2020) 13637–13649. https://doi.org/10.1039/D0CP00446D.
503 504 505	[32]	W. Luo, K.J. Gross, A kinetics model of hydrogen absorption and desorption in Ti-doped NaAlH4, J. Alloys Compd. 385 (2004) 224–231. https://doi.org/10.1016/J.JALLCOM.2004.05.004.
506 507	[33]	L. Greenspan, Humidity Fixed Points of Binary Saturated Aqueous Solutions, J. Res. Natl. Bur. Stand A. Phys Ics Chem. 82A (1976) 89–96.
508 509	[34]	M.A. Stanish, D.D. Perlmutter, Rate processes in cycling a reversible gas-solid reaction, AIChE J. 30 (1984) 56–62. https://doi.org/10.1002/aic.690300110.
510 511 512	[35]	L. Favergeon, M. Pijolat, Influence of water vapor pressure on the induction period during Li 2SO4·H2O single crystals dehydration, Thermochim. Acta. 521 (2011) 155–160. https://doi.org/10.1016/j.tca.2011.04.018.
513 514 515	[36]	L. Okhrimenko, L. Favergeon, K. Johannes, F. Kuznik, New kinetic model of the dehydration reaction of magnesium sulfate hexahydrate: Application for heat storage, Thermochim. Acta. 687 (2020) 178569. https://doi.org/10.1016/J.TCA.2020.178569.
516 517	[37]	A.K. Galwey, Magnitudes of Arrhenius parameters for decomposition reactions of solids, Thermochim. Acta. 242 (1994) 259–264. https://doi.org/10.1016/0040-6031(94)85030-5.
518 519	[38]	I.V.S.Y. V.S., Database of Thermal Constants of Substances, (n.d.). http://www.chem.msu.ru/cgi-bin/tkv.pl.
520		
521		